

# On-chip magnon polaritons in the ultrastrong coupling regime

Shugo Yoshii<sup>1,2†</sup>, Manuel Müller<sup>3,4</sup>, Ryo Ohshima<sup>1,2</sup>, Matthias Althammer<sup>3,4</sup>,

Yuichiro Ando<sup>1,2,5</sup>, Hans Huebl<sup>3,4,6</sup>, and Masashi Shiraishi<sup>1,2\*</sup>

<sup>1</sup>Department of Electronic Science and Engineering, Kyoto University, Nishikyo-ku, Kyoto 615-8510, Japan

<sup>2</sup>Center for Spintronics Research Network, Institute for Chemical Research, Kyoto University, Uji, Kyoto 611-0011, Japan

<sup>3</sup>Walther-Meißner-Institut, Bayerische Akademie der Wissenschaften, 85748 Garching, Germany

<sup>4</sup>Technical University of Munich, TUM School of Natural Sciences, Physics Department, 85748 Garching, Germany

<sup>5</sup>Department of Physics and Electronics, Osaka Metropolitan University, 1-1 Gakuencho, Sakai, Osaka 599-8531, Japan

<sup>6</sup>Munich Center for Quantum Science and Technology (MCQST), 80799 Munich, Germany

†Shugo Yoshii, Email address: yoshii.shugo.x63@kyoto-u.jp

\*Masashi Shiraishi, Email address: shiraishi.masashi.4w@kyoto-u.ac.jp

**Light-matter interactions underpin the quantum technologies from quantum information processing to quantum sensing. When the coupling strength of light-matter interactions approaches the resonance frequencies of light and matter – the ultrastrong coupling regime – antiresonant (counter-rotating) processes, in which a photon and a matter excitation are simultaneously created or annihilated, induce non-negligible ground-state quantum entanglement between light and matter. Ultrastrong coupling thus provides a robust platform for noise-tolerant quantum entanglement, essential for reliable quantum technologies. However, the diamagnetic term typically counteracts antiresonant interactions, inhibiting intriguing phenomena such as thermal equilibrium superradiant phase transitions. Here, we present an on-chip platform consisting of a superconducting resonator and thin ferromagnetic films achieving ultrastrong magnon-photon coupling system (magnon polaritons) via collective magnetic-dipole interactions, significantly circumventing the diamagnetic term. We experimentally demonstrate a pronounced Bloch-Siegert shift of about 60 MHz – direct evidence of antiresonant interactions – and**

**observe cooperative enhancement of the effective coupling strength through increasing the number of remote magnon elements coupling with one photon mode. This scalable platform facilitates exploration of exotic quantum phenomena driven by antiresonant interactions, bridging spintronics and quantum optics, and enabling noise-tolerant quantum technological applications.**

## Main text

Light–matter interactions are one of the most fundamental concepts of quantum science, underpinning technologies ranging from quantum information processing to quantum sensing. Once light and matter strongly couple with each other, they begin to coherently exchange energy, forming states known as coherent hybrid states. These coherent hybrid states mix the states of light and matter, enabling emergent dynamics which play a pivotal role in modern physics applications including quantum information processing<sup>1–4</sup>. Antiresonant processes in light-matter interactions, characterized by the simultaneous creation or annihilation of a photon and a excitation of matter (known as counter-rotating terms in the Hamiltonian; see Methods for details), facilitate intriguing quantum effects – such as two-mode squeezed ground states<sup>5,6</sup>, virtual photon generation<sup>7–9</sup>, and equilibrium superradiant phase transitions<sup>10,11</sup> – offering vital opportunities for deepening quantum science and achieving noise-tolerant quantum technology, including fast and robust quantum information technologies and quantum computation<sup>12</sup>. Typically, counter-rotating terms are neglected under conventional strong coupling conditions where the rotating-wave approximation (RWA) remains valid; however, when the coupling strength exceeds approximately 10% of individual resonance frequencies, the system enters the ‘ultrastrong’ coupling regime, making the previously negligible counter-rotating terms highly significant. Consequently, experimental platforms capable of reliably reaching ultrastrong coupling regimes have emerged as particularly promising environments for establishing innovative, noise-tolerant quantum technologies.

Ultrastrong light–matter coupling has been demonstrated in several platforms, notably circuit quantum electrodynamics (c-QED) using Josephson junctions<sup>13–15</sup> and semiconductor microcavities hosting Landau polaritons<sup>16–18</sup>. Further exploration of the intriguing physics induced by counter-rotating terms, however, is constrained by the  $A^2$  (diamagnetic) term in the Hamiltonian inherent to electric-dipole interactions illustrated in Fig. 1a, enforcing the no-go theorem of equilibrium superradiant phase transitions<sup>19,20</sup>. By contrast, Zeeman coupling in magnetic-dipole interactions, depicted in Fig. 1b, between cavity photons and collective spin excitations (magnons) does not involve interactions due to the charge dynamics and enables circumventing the  $A^2$  term<sup>21–24</sup>. Although an individual spin weakly couples to a photon, the collective coupling  $g \propto \sqrt{N/V_p}$ ,

where  $N$  is the total number of spins and  $V_p$  is the photon volume, can be significantly enhanced through cooperative coupling (Dicke cooperativity) and by concentrating the microwave field using superconducting resonators. This enables strong magnon-photon coupling state (magnon polaritons) even in compact, integrated on-chip devices based on thin ferromagnetic films<sup>25–28</sup>, forming magnon-polariton c-QED systems. These magnon-polariton c-QED platforms thus present promising candidates for achieving ultrastrong coupling without the limitations of the  $A^2$  term. Nevertheless, definitive signatures of counter-rotating terms, such as the energy shift due to the presence of counter-rotating terms (Bloch-Siegert shift)<sup>14,29</sup>, or a quantitative suppression of the  $A^2$  term, have remained elusive. Moreover, ultrastrong magnon-photon coupling to date has predominantly employed bulk ferromagnetic materials<sup>30,31</sup>, leaving a pivotal question regarding scalable device-integration strategies unanswered. A platform that addresses these challenges would propel ultrastrong-coupling physics to the next stage, laying essential groundwork for noise-tolerant quantum technologies merging spintronics and quantum optics.

Here, we experimentally demonstrate ultrastrong magnon-photon coupling with clear counter-rotating term dynamics, indicated by the Bloch-Siegert shift. Our system (Fig. 2a) is a planar cavity-magnonic device integrating a ferromagnetic NiFe (permalloy) 30 nm thin film in the form of multiple isolated stripes, with a meander-type high- $T_C$  (YBa<sub>2</sub>Cu<sub>3</sub>O<sub>7</sub>, i.e. YBCO) superconducting microwave resonator. The Kittel magnon modes of NiFe stripe elements collectively couple with the photon mode, pushing the magnon-photon interaction into the ultrastrong coupling regime. We directly observe a Bloch-Siegert shift and quantify a suppression of the  $A^2$  term to  $\approx 5\%$  of the electric-dipole coupling, thereby circumventing the conventional no-go theorem of superradiant phase transition and providing the critical coupling strength to achieve a superradiant phase transition by increasing the effective coupling strength. The effective coupling strength scales with  $\sqrt{n}$ , where  $n$  is the number of permalloy elements, confirming Dicke cooperativity in our system. The Bloch-Siegert shift is tunable via the bright-mode cooperativity in excellent agreement with theory. Our approach establishes a scalable, lithographically-defined platform for studying exotic physical phenomena in ultrastrong coupling

regime and for merging spintronics with quantum optics at accessible tens of Kelvin temperatures, offering inviting routes to future device applications.

### **Magnon polaritons in FM stripes mounted on a YBCO superconducting resonator**

Strong photon confinement in superconducting resonators offers a promising route to realize large effective coupling strengths in magnon-photon interactions, owing to the reduced photon volume ( $V_p$ ). The effective coupling strength between a magnon mode in a ferromagnet and the photon mode ( $g_0$ ) is given by<sup>26,32</sup>:

$$g_0 = g_s \sqrt{N}, \quad (1)$$

where  $g_s$  denotes the coupling strength between a single Bohr magneton and the photon, and  $N$  is the total number of spins in the ferromagnet.  $g_s$  is proportional to  $1/\sqrt{V_p}$ , on-chip superconducting resonators with diminished photon volumes can substantially enhance  $g_s$ , making it possible to observe magnon polaritons even in thin ferromagnetic films with small magnetic volumes<sup>27,28</sup>. The uniform magnetization precession in a thin ferromagnetic film (the so-called Kittel magnon mode) interacts with the AC magnetic field of microwave photon resonator. For a sufficiently large magnetic moment, the interaction between the vacuum fluctuations of the microwave resonator and the magnetic modes becomes strong, exchanging energy in a coherent manner and forming hybrid magnon–photon states known as magnon polaritons.

Here, we fabricate a lumped-element superconducting resonator from the high- $T_c$  superconductor, YBCO, incorporating a meander-shaped inductor (Fig. 2a) with permalloy stripes. This design supports a strongly confined and uniform AC microwave magnetic field on the inductor surface (see Methods) and achieves a quality factor of approximately 3600 (Fig. 2b). YBCO is a type-II superconductor and thus shows high resilience against external magnetic fields and principally operates up to the critical temperature of 90 K (see Supplemental information). This enables the clear observation of magnon-photon hybridization for applied magnetic fields of 150 mT and moderate temperatures of 10 K.

The patterned 30 nm-thick permalloy stripes in these hybrid systems host collective magnon modes that couple via Zeeman interaction to the photon mode in a YBCO resonator. Figure 2c presents the transmission spectra normalized to a reference traces ( $|\Delta S_{21}|$ ) taken at  $\mu_0 H = 30$  mT for the resonator with 26 permalloy stripes in a YBCO chip (YBCO#1) as a function of the external positive magnetic field. Figures 2d-f show the enlarged spectra for 0, 7, and 14 mT with the fitting result of Eq. (5), respectively. Note that the larger linewidth of the spectra can be attributed to the larger magnon damping than photon damping (see the details in Methods). These spectra exhibit characteristic field dependence of the microwave resonance frequency, anticrossing spectra between magnon and photon modes, which is indicative of magnon-photon hybridization.

The Hopfield Hamiltonian effectively describes magnon polaritons exhibiting ultrastrong coupling with  $A^2$  term<sup>31</sup>. Within a quantum mechanical formalism, the magnon-polariton frequencies  $\omega_{\text{mp}}^{\pm}$  are determined by solving the following quartic equation (see Methods for the derivation)

$$\omega_{\text{mp}}^{\pm 4} - \omega_{\text{mp}}^{\pm 2}(\omega_{\text{m}}^2 + \omega_{\text{p}}^2 + 4D\omega_{\text{p}}) + \omega_{\text{m}}^2\omega_{\text{p}}^2 + 4D\omega_{\text{m}}^2\omega_{\text{p}} - 4\omega_{\text{m}}^2G_{\text{eff}}^2 = 0, \quad (2)$$

where  $G_{\text{eff}}$  is the effective coupling strength between magnons and photons,  $\omega_{\text{p}}$  is defined as the resonance frequency of the notch-type lumped-element resonator, and  $\omega_{\text{m}} = \gamma\mu_0\sqrt{H(H + M_{\text{eff}})}$  represents the Kittel mode frequency dependent on the external magnetic field  $H$ . Here,  $\gamma$  is the gyromagnetic ratio,  $\mu_0$  is the vacuum permeability, and  $M_{\text{eff}}$  is the effective magnetization. For the evaluation of the diamagnetic coefficient  $D$  in our system, we assume  $D = \beta/\omega_{\text{m}}$ , where  $\beta$  is diamagnetic coefficient. This assumption allows a systematic comparison to the diamagnetic term predicted by the Thomas-Reiche-Kuhn (TRK) sum rule ( $D_{\text{TRK}} = G_{\text{eff}}^2/\omega_{\text{m}}$ )<sup>12</sup>. Such a comparison facilitates examining the potential breakdown of the conventional no-go theorem, typically valid for electric-dipole systems, in magnetic-dipole systems.

The RWA typically breaks down in the ultrastrong coupling regime, where counter-rotating terms become significant. Figure 2g also represents the fitting result with extracted coupling parameters:  $\omega_{\text{p}}/2\pi = 5.041$  GHz,  $\mu_0 M_{\text{eff}} = 1.108$  T, and  $G_{\text{eff}}/2\pi = 512.3$  MHz. These parameters yield a  $G_{\text{eff}}/\omega_{\text{p}}$  ratio of 0.101, exceeding the widely accepted threshold (0.1) that defines the ultrastrong coupling regime<sup>12</sup>. The presence of counter-rotating terms modifies the polariton energy spectrum, manifesting as the Bloch-Siegert shift ( $\Delta f_{\text{BS}}$ )<sup>29</sup>. This shift provides direct experimental evidence for counter-rotating terms in strongly coupled systems and can

be identified by deviations in dispersion curves obtained through quantum mechanical framework<sup>14,33,34</sup>. To elucidate this effect, we simulated magnon-polariton spectra based on a Hamiltonian (see Eq. (12) in Methods), explicitly comparing cases with and without counter-rotating terms (Figs. 2h and i; see Methods for further details on dispersion calculations). The difference between two simulated spectra directly quantifies  $\Delta f_{\text{BS}}$ , aligning closely with our experimental observations and conclusively demonstrating the presence of counter-rotating terms.

Magnon-polariton systems inherently suppress the  $A^2$  term due to their dominant magnetic-dipole coupling, distinct from the minimal coupling inherent to electric-dipole interactions<sup>21–24</sup>. The fitting result represented in Fig. 2c yields the estimated diamagnetic coefficient  $\beta = (4.89 \pm 0.46) \times 10^{17} \text{ (rad} \cdot \text{Hz)}^2$ , corresponding to a diamagnetic term  $D = 2.46 \text{ MHz}$  at the vacuum splitting condition  $\omega_p = \omega_m$ . By comparing this result with the diamagnetic term predicted by TRK sum rule conventionally applied in electric-dipole coupling, we find a suppression factor  $B = D/D_{\text{TRK}} \sim 0.05$ , which confirms significant suppression of the diamagnetic term in magnon-polariton systems in thin ferromagnetic films, consistent with observations made in ferrimagnetic insulators such as  $\text{Y}_3\text{Fe}_5\text{O}_{12}$  (YIG)<sup>31</sup>.

Figures 2h and 2i further illustrate simulated spectra derived from the Hamiltonian excluding the diamagnetic term (the Dicke Hamiltonian), showing excellent agreement with experimental spectra at magnetic fields away from zero. These findings strongly suggest that around the vacuum splitting condition, magnon polaritons in the ultrastrong coupling regime effectively conform to the Dicke Hamiltonian, where counter-rotating terms responsible for squeezed magnon-photon states remain significant. Moreover, the critical coupling strength required for a superradiant phase transition is determined by:

$$G_c^2(B) = G_c^2(0) \frac{1}{1-B}, \quad (3)$$

where  $G_c(0) = \sqrt{\omega_p \omega_m}/2$  is the conventional critical coupling strength for the Dicke Hamiltonian<sup>6,20</sup>. For the  $B = 0.05$ , the critical coupling strength  $G_c$  is approximately 2.59 GHz, nearly five times greater than the effective coupling strength experimentally estimated as shown in Fig. 2g. In subsequent discussions, the Dicke

model will be utilized to analyze the lower polariton branch of the observed frequencies to precisely estimate coupling parameters.

### Dicke cooperativity in the coupling of collective magnon modes and photon mode

To date, the coupling strength between magnons and photons has primarily been enhanced by increasing either the total number of spins or the vacuum fluctuation amplitude of the photon mode. Here, we introduce another key to significantly enhance  $G_{\text{eff}}$  by employing a system comprising a single uniform photonic mode coupled to multiple collective magnon modes in thin ferromagnetic films. Each individual magnon mode couples to the photon mode with a coupling strength  $g_0$  (see Fig. 3a). Considering the collective bright magnon mode formed from these individual magnon modes, the interaction Hamiltonian  $\mathcal{H}_{\text{int}}$  for the magnon-photon coupling can be expressed as:

$$\mathcal{H}_{\text{int}} = \hbar G_{\text{eff}} (\hat{a}^\dagger \widehat{M}_B + \hat{a} M_B^\dagger + \hat{a}^\dagger M_B^\dagger + \hat{a} \widehat{M}_B). \quad (4)$$

Here  $G_{\text{eff}} = g_0 \sqrt{n}$ , where  $n$  is the number of the permalloy elements,  $\hat{a}$  ( $\hat{a}^\dagger$ ) is the annihilation (creation) operator of photons, and  $\widehat{M}_B$  ( $M_B^\dagger$ ) is annihilation (creation) operator of a collective magnon bright mode. Notably, the bright magnon mode exhibits a cooperative enhancement of the coupling strength, characterized by a  $\sqrt{n}$  scaling, which equally affects both rotating and counter-rotating terms. This collective enhancement aligns with the theoretical prediction of cooperative interactions described by Dicke<sup>35</sup>.

Following Eq. (4), the effective coupling strength  $G_{\text{eff}}$  scales proportionally to the square root of the number  $n$  of permalloy stripes coherently coupled to the photon mode, leading to cooperative enhancement. To verify this scaling behavior experimentally, we prepared two YBCO chips (labeled YBCO#1 and YBCO#2), each incorporating resonators patterned with varying numbers of permalloy stripes ( $n = 1, 8, 16, 26$  for YBCO#1, and  $n = 1, 26$  for YBCO#2). The normalized transmission spectra of YBCO#1 chip, displayed in Figs. 3d-e, reveal distinct magnetic field-dependent behavior characteristic of magnon-photon coupling. By fitting the lower polariton branch of each spectrum using the Dicke model, we extracted the  $n$ -dependence of  $G_{\text{eff}}$ . Given that the single-Bohr-magneton coupling  $g_s$  is proportional to the square root of the uncoupled photon resonance frequency,  $f_p$ <sup>32</sup>, we introduce a normalized coupling strength  $\varepsilon = G_{\text{eff}}/2\pi\sqrt{f_p}$ , which should scale as  $\sqrt{n}$ .

Figure 3f indeed confirms this linear relationship, with fitted slopes  $\alpha = 1520 \sqrt{\text{Hz}}$  for YBCO#1 and  $\alpha = 1791 \sqrt{\text{Hz}}$  for YBCO#2. This clearly demonstrates that the observed enhancement in  $G_{\text{eff}}$  originates from the formation of a collective magnon bright mode, consistent with Dicke cooperativity. The observed variation in the coupling coefficient  $\alpha$  between YBCO#1 and YBCO#2 likely arises from differences in single-Bohrmagneton coupling  $g_s$ , since  $\alpha = g_0 / \sqrt{f_p} \propto g_s$ , where  $g_s(\text{YBCO\#1}) \approx 28.4 \text{ Hz}$  and  $g_s(\text{YBCO\#2}) \approx 35.8 \text{ Hz}$ . This discrepancy may be attributed to variations in surface roughness between the YBCO chips (see Supplementary Information).

### $G_{\text{eff}}$ -dependence of Bloch-Siegert shift

According to Eq. (4), the counter-rotating terms ( $\hat{a}^\dagger M_B^\dagger + \hat{a} \widehat{M}_B$ ) induce a Bloch-Siegert shift—a characteristic frequency shift in the magnon-polariton modes<sup>14,29,33</sup>, whose magnitude is controllable by altering the number of participating magnon modes. Demonstrating a Dicke-cooperative enhancement of this Bloch-Siegert shift constitutes compelling evidence for the presence and significance of counter-rotating interactions between magnons and photons, even within single-mode magnons. Figure 4a illustrates the  $\Delta f_{\text{BS}}$  as a function of external magnetic fields for resonators comprising varying numbers of permalloy stripes. The data clearly exhibit larger frequency shifts for resonators with more stripes, reflecting an increase in the  $G_{\text{eff}}$ . These results experimentally confirm theoretical predictions<sup>36</sup>, demonstrating that  $\Delta f_{\text{BS}}$  scales positively with  $G_{\text{eff}}$ , achieved by increasing the number of permalloy elements. The enhancement of  $\Delta f_{\text{BS}}$  at higher magnetic fields is attributed to an increase in virtual photon excitations induced by counter-rotating terms within the regime of  $\omega_p / \omega_m \ll 1$ <sup>37</sup>.

Moreover, the Dicke cooperativity of collective magnon modes enhances the effective coupling strength  $G_{\text{eff}}$ , thereby increasing  $\Delta f_{\text{BS}}$ , and thus validating the theoretical interaction Hamiltonian described in Eq. (4). Under the lowest-order approximation, theory predicts the Bloch-Siegert shift to scale as  $\Delta f_{\text{BS}} \propto G_{\text{eff}}^2 / \omega_p$ . Figure 4b plots the measured  $\Delta f_{\text{BS}}$  against  $G_{\text{eff}}^2 / f_p$  at magnetic fields of 65 mT, 100 mT, and 140 mT. The linear dependencies observed confirm the theoretical scaling relationship  $\Delta f_{\text{BS}} \propto G_{\text{eff}}^2 / \omega_p$ . From

linear fits to the experimental data, the slope coefficients  $C$  are determined as be  $-0.617 \pm 0.012$  at 65 mT,  $-0.655 \pm 0.006$  at 100 mT, and  $-0.694 \pm 0.005$  at 140 mT. Despite variations in the intrinsic magnon and photon relaxation rate across systems, the Bloch-Siegert shift is consistently governed by coupling strength and resonance frequency, supporting theoretical assertions that the population of virtual photons arising from counter-rotating terms remains unaffected by relaxation processes<sup>9</sup>.

## Discussion and Outlook

Magnons have garnered considerable interest as promising media for next-generation information technologies, primarily owing to their tunability<sup>38</sup>, nonlinearity<sup>39</sup>, nonreciprocity<sup>40</sup>, and intrinsic non-Hermitian dynamics<sup>41</sup>. Moreover, magnons can be efficiently converted into spin and charge currents through interfacial spin-orbit coupling. The spin currents generated through this mechanism can encode and transmit quantum information intrinsic to magnons<sup>42–45</sup>, providing a promising route to explore entangled quantum states arising from counter-rotating terms in magnon-photon interactions. Accessing even stronger coupling regimes – such as deep-strong coupling – could be feasible by optimizing the coupling strength  $g_s$  through advanced photonic architectures<sup>28</sup>, by utilizing high-spin-density ferromagnetic materials, like CoFe thin films<sup>46</sup> or by harnessing the cooperative enhancement of separated ferromagnetic elements demonstrated in this work. Many proposed approaches for integrating magnonics into ultrastrong coupling phenomena can readily be implemented in our system by leveraging the Dicke cooperativity arising from collective magnon modes.

The significantly suppressed, but still finite  $A^2$  term in the Hopfield Hamiltonian – an unexpected feature in magnon-photon interactions – merits careful examination. Controlling this term is critical for realizing superradiant phase transitions under strong light-matter coupling by circumventing the no-go theorem, which typically prohibits such transitions in the presence of an  $A^2$  term. In principle, the  $A^2$  term arises from minimal coupling within electron-based-dipole interactions (see the details in Supplemental Information No.7)<sup>19</sup>. Therefore, the finite diamagnetic term observed in Fig. 2h suggests a notable electronic contribution to the photon component in magnon polaritons. In contrast to previous studies on ultrastrongly coupled magnon

polaritons in insulating YIG ferromagnets – where the insulating nature significantly reduces the magnitude of the  $A^2$  shift<sup>31</sup> – the finite  $A^2$  term identified in permalloy may originate from electron-mediated interactions, including electron-magnon or electron-photon coupling. Given that itinerant electrons play the crucial role of orbital angular momentum in ferromagnets, quantitative evaluation of the  $A^2$  term may provide essential insights into orbitronic phenomena. Although systematic material-controlled experiments and theoretical frameworks explicitly accounting for electron contributions in ferromagnets will be indispensable to comprehensively elucidate the precise mechanism underlying the  $A^2$  term in magnon-polariton systems, pursuing this research direction promises not only fundamental insights into the  $A^2$  term essential for achieving thermal equilibrium superradiant phase transition but also novel methods to probe orbital dynamics in ferromagnets, addressing longstanding challenges in spintronics.

## Methods

**Preparation of superconducting resonators.** The 150 nm-thick YBCO films, capped with a 40 nm-thick Au layer and deposited on sapphire substrates with dimensions of 6 mm × 10 mm, were sourced commercially. The YBCO chips consist of a single feedline coupled to five lumped-element resonators with varying resonance frequencies (see the Supplemental Information). These structures were patterned using electron-beam lithography, with the interdigital finger systematically modified across each resonator to tune their frequencies. The parameter of the resonator structure, as shown in Extended data Fig. 1a, is in the extended table 1, where  $l_c$  is varied to tune the resonance frequency. The resonators are labelled R1 through R5, corresponding to increasing resonance frequencies. Subsequently, the YBCO and Au layers were etched using Ar ion milling to define the resonator patterns. The Au capping layer on the resonators was completely removed by an additional Ar ion milling step to suppress the eddy current loss in Au layer.

**Integration of Thin Ferromagnetic Stripes onto YBCO resonators.** A 30 nm-thick permalloy ( $\text{Ni}_{80}\text{Fe}_{20}$ ) layer, patterned into stripes aligned with the inductor segments of the lumped-element resonators, was deposited on the YBCO resonators via electron-beam evaporation. To ensure electrical insulation, a 10 nm-thick  $\text{SiO}_2$  buffer layer was first sputtered onto the surface. The full multilayer structure of the ferromagnetic stripes follows the stacking sequence:  $\text{SiO}_2$  (10 nm) / MgO (2 nm) / Permalloy (30 nm) / Ti (3 nm) (see Fig. 2a) with the geometry of  $15 \mu\text{m} \times 400 \mu\text{m}$ .

**Transmission measurements.** The YBCO chips containing the resonator structures were placed in a low-temperature cryostat system, with RF cables connected to a vector network analyzer (VNA) (see Extended Data Fig. 1). Transmission spectra,  $S_{12}$ , were measured as a function of the external magnetic field, with the temperature held constant at 10 K. Here the transmission spectra are attenuated with 20 dB before and 6 dB after the YBCO chip, with a 18 dB amplification on the detection side. The external magnetic field was varied within a range of  $\pm 145$  mT. The normalized transmission spectra,  $|\Delta S_{12}|$ , were calculated by dividing  $S_{12}$  by the

transmission spectrum measured at a magnetic field where no magnon-polariton peaks were observed, such as at 30 mT. This normalization effectively removes background contributions from environmental noise, isolating the relevant spectral features of the resonators.

**Modelling the notch-type resonators.** Using input-output formalism, the transmission spectra of the notch-type resonator structure can be expressed as following:

$$S_{21}(f) = \frac{\tilde{V}_2}{\tilde{V}_1} = ae^{i\beta}e^{-2\pi if\tau} \left[ 1 - \frac{(Q/|Q_{\text{ext}}|)e^{i\phi}}{1 + 2iQ(\frac{f}{f_r} - 1)} \right], \quad (5)$$

$$Q = \left( \frac{1}{Q_{\text{ext}}} + \frac{1}{Q_{\text{int}}} \right)^{-1}, \quad (6)$$

where  $ae^{i\beta}e^{-2\pi if\tau}$  is the environment coefficient arising from the measurement system, excluding the resonator contribution. The term inside the square brackets represents the resonator response, incorporating an additional phase correction  $e^{i\phi}$ . The resonance frequency  $f_r$  is given by  $1/\sqrt{LC}$ . The  $Q_{\text{int}}$  and  $Q_{\text{ext}}$  correspond to the internal quality factor of the resonator and the external quality factor related to the capacitive coupling between the resonator and the feedline, respectively. The magnon polariton frequency  $f_{\text{mp}}$  can be estimated by Eq. (5) as a function of the external magnetic field.

The homogeneous AC magnetic field is excited on the inductor part of this type of lumped element superconducting resonator<sup>49</sup>. We perform finite-element simulations to map the field magnitude. The resulting profile reveals pronounced confinement of the photon mode within a few micrometers, which underpins an enhanced single-spin coupling strength.

**Kittel mode ( $k = 0$  magnon mode).** The magnon mode with the uniform magnetization precession ( $k = 0$ ) in thin ferromagnetic films with in-plane external magnetic field is expressed by the Kittel formula as follows:

$$f_m = \frac{\gamma\mu_0}{2\pi} \sqrt{H(H + M_{\text{eff}})}. \quad (7)$$

Here,  $\gamma$ ,  $\mu_0$ , and  $M_{\text{eff}}$  are gyromagnetic ratio of ferromagnetic materials, the vacuum permeability, and the effective magnetization, respectively. In this mode, all the magnetic moment precesses in phase, resulting in a collective oscillation of the magnetization in thin ferromagnetic films without the spatial variation unlike  $k \neq 0$  magnons. Considering the FEM result of excited AC magnetic field in this superconducting resonator<sup>49</sup>, Kittel mode is excited in phase in the ferromagnetic stripes mounted on the meander structure of the superconducting resonator.

**Coupling Hamiltonian between one photon mode and collective magnon modes.** The total Hamiltonian describing the coupling between a photon mode and collective magnon modes is effectively captured by the Hopfield model<sup>50</sup> without invoking the rotating wave approximation:

$$\widehat{\mathcal{H}} = \hbar\omega_p \widehat{a}^\dagger \widehat{a} + \hbar \sum_i \omega_i \widehat{m}_i^\dagger \widehat{m}_i + \hbar \sum_i g_i (\widehat{a}^\dagger + \widehat{a}) (\widehat{m}_i^\dagger + \widehat{m}_i) + \hbar D (\widehat{a}^\dagger + \widehat{a})^2. \quad (8)$$

Here,  $\omega_p$  denotes the uncoupled photon resonance frequency,  $\omega_i$  are the uncoupled resonance frequencies of the  $i$ -th magnon mode, described by the Kittel formula, and  $D$  is the diamagnetic coefficient representing the so-called  $A^2$  term. When each magnon mode oscillates coherently at frequency  $\omega_i = \omega_m$  as illustrated in Fig. 3a, these modes form a collective bright mode, represented by the operator<sup>51</sup>:

$$\widehat{M}_B = \frac{1}{G} \sum_i g_i \widehat{m}_i, \quad (9)$$

$$G_{\text{eff}} = \sqrt{\sum_i |g_i|^2} = g_0 \sqrt{n}, \quad (10)$$

where  $n$  is the total number of magnon modes, and  $G_{\text{eff}}$  is the effective coupling strength between the collective bright magnon mode and the photon mode. By substituting Eqs. (9) and (10) into Eq. (8), the interaction Hamiltonian (the third term in Eq. (8)) can be expressed as:

$$\mathcal{H}_{\text{int}} = \hbar G_{\text{eff}} (\widehat{a}^\dagger \widehat{M}_B + \widehat{a} M_B^\dagger + \widehat{a}^\dagger M_B^\dagger + \widehat{a} \widehat{M}_B). \quad (11)$$

To evaluate the coupling parameters at low frequencies around  $\omega_m$ , we redefine the effective coupling as  $G'_{\text{eff}} = G_{\text{eff}} \sqrt{\frac{\omega_m}{\omega_p}}$ . Thus, the Hamiltonian describing interactions between the photon mode and bright magnon modes becomes:

$$\mathcal{H} = \hbar\omega_p \widehat{a}^\dagger \widehat{a} + \hbar\omega_m \widehat{M}_B^\dagger \widehat{M}_B + \hbar G'_{\text{eff}} (\widehat{a}^\dagger \widehat{M}_B + \widehat{a} M_B^\dagger + \widehat{a}^\dagger M_B^\dagger + \widehat{a} \widehat{M}_B) + \hbar D (\widehat{a}^\dagger + \widehat{a})^2, \quad (12)$$

Here, we ignore magnon dark modes since they are decoupled from the photon mode and thus do not contribute significantly to the observed coupling phenomena.

Diagonalization of the Hamiltonian in Eq. (12) can be achieved through the Hopfield-Bogoliubov transformation, employing the operator vector  $v^\dagger = [\hat{a}^\dagger \quad \widehat{M}_B^\dagger \quad \hat{a} \quad \widehat{M}_B]$ , as follows<sup>34</sup>:

$$\mathcal{H} = \frac{1}{2} [\hat{a}^\dagger \quad \widehat{M}_B^\dagger \quad \hat{a} \quad \widehat{M}_B] \begin{bmatrix} \omega_p + 2D & G'_{\text{eff}} & 2D & G'_{\text{eff}} \\ G'_{\text{eff}} & \omega_m & G'_{\text{eff}} & 0 \\ 2D & G'_{\text{eff}} & \omega_p + 2D & G'_{\text{eff}} \\ G'_{\text{eff}} & 0 & G'_{\text{eff}} & \omega_m \end{bmatrix} \begin{bmatrix} \hat{a} \\ \widehat{M}_B \\ \hat{a}^\dagger \\ \widehat{M}_B^\dagger \end{bmatrix}. \quad (13)$$

Introducing polariton operators, defined as linear combinations of photon and bright magnon mode operators,  $\hat{p}^\pm = \alpha^\pm \hat{a} + \beta^\pm \widehat{M}_B + \gamma^\pm \hat{a}^\dagger + \delta^\pm \widehat{M}_B^\dagger$ , the Hamiltonian in Eq. (13) is diagonalized in terms of polariton frequencies as:

$$\mathcal{H} = \omega_{\text{mp}}^+ \hat{p}^{+\dagger} \hat{p}^+ + \omega_{\text{mp}}^- \hat{p}^{-\dagger} \hat{p}^-, \quad (14)$$

which satisfies the eigenvalue equation  $[\hat{p}^\pm, \mathcal{H}] = \omega_{\text{mp}}^\pm \hat{p}^\pm$ . Therefore, solving the eigenvalue problem of the Hopfield matrix  $M$ , explicitly given by:

$$M = \begin{bmatrix} \omega_p + 2D & G'_{\text{eff}} & 2D & G'_{\text{eff}} \\ G'_{\text{eff}} & \omega_m & G'_{\text{eff}} & 0 \\ 2D & G'_{\text{eff}} & \omega_p + 2D & G'_{\text{eff}} \\ G'_{\text{eff}} & 0 & G'_{\text{eff}} & \omega_m \end{bmatrix} \begin{bmatrix} 1 & 0 & 0 & 0 \\ 0 & 1 & 0 & 0 \\ 0 & 0 & -1 & 0 \\ 0 & 0 & 0 & -1 \end{bmatrix}. \quad (15)$$

yields the magnon-polariton frequencies  $\omega_{\text{mp}}^\pm$ . The contributions of the counter-rotating and diamagnetic terms can be selectively excluded, depending on the approximation required. Approximate analytical expressions for other polariton branches are provided in the Supplemental Information.

### Evaluation of spin coupling strength per Bohr magneton $g_s$ in YBCO#1 and YBCO#2.

To further characterize the YBCO resonator's performance, we evaluated the coupling strength per Bohr magneton ( $g_s$ ). The total number of electron spins in a permalloy stripe with the geometry of  $15 \mu\text{m} \times 400 \mu\text{m}$  – determined by using a saturation magnetization of permalloy;  $\mu_0 M_s = 1 \text{ T}^{27}$  – is  $1.55 \times 10^{13}$ , leading to  $g_s \approx 28.4 \text{ Hz}$  for YBCO#1 and  $g_s \approx 35.8 \text{ Hz}$  for YBCO#2 from Eq. (1). They are obtained in resonators with one permalloy element in each YBCO chip by fitting the lower branch spectra with Dicke model. Here,

we assume the same spin number with each permalloy element. Notably, these value values exceed the  $\sim 20$  Hz reported for CPW resonators in previous studies<sup>27,28</sup>, demonstrating a enhancement attributed to the optimized lumped-element resonator design, which features carefully engineered capacitor and inductor geometries.

**Critical coupling strength for superradiant phase transition.** We derive the critical coupling at which our magnon-polariton platform enters the superradiant phase while the  $A^2$  term is partially suppressed. Following Nataf and Ciuti<sup>20</sup>, the quantum critical point occurs when one polariton branch softens to zero energy, i.e. when  $\det(M) = 0$ . For the bilinear Hamiltonian considered here, the determinant is

$$\det(M) = \omega_p \omega_m (4D\omega_m - 4G_{\text{eff}}'^2 + \omega_p \omega_m). \quad (16)$$

Substituting  $D = B G_{\text{eff}}'^2 / \omega_m$  into Eq. (16) and imposing  $\det(M) = 0$  yields the critical coupling

$$G_c^2(B) = \frac{\omega_p \omega_m}{4} \frac{1}{1 - B}. \quad (17)$$

Hence, the condition of  $0 \leq B < 1$  provides the finite critical coupling  $G_c$ , although in the TRK sum rule limit  $B \rightarrow 1$  the critical coupling diverges,  $G_c \rightarrow \infty$ , reinstating the no-go theorem that forbids a superradiant phase transition in the presence of an unsuppressed  $A^2$  term<sup>19,20</sup>.

**Analysis of spectra with relaxation rate of magnons and photons.** To investigate the relaxation rate of magnons and photons, we analyze the magnon-polariton modes by explicitly including the respective relaxation rates for magnons ( $\kappa_m$ ) and photons ( $\kappa_p$ ). These relaxation rates of magnons and photons, which can be characterized via an input-output formalism<sup>27</sup>, play a crucial role in evaluating cooperativity and decoherence time of the system and discussing non-Hermitian physics<sup>41</sup>. We adopt a simplified Tavis–Cummings model that neglects both counter-rotating terms and the diamagnetic term, resulting in the effective Hamiltonian considering  $\kappa_m$  and  $\kappa_p$ :

$$\mathcal{H} = \hbar(\omega_p - i\kappa_p)\hat{a}^\dagger \hat{a} + \hbar(\omega_m - i\kappa_m)\widehat{M}_B^\dagger \widehat{M}_B + \hbar G_{\text{eff}} (\hat{a}^\dagger \widehat{M}_B + \hat{a} \widehat{M}_B^\dagger). \quad (18)$$

The corresponding Heisenberg equations of motion for the annihilation operators  $\hat{a}$  (photon mode) and  $\widehat{M}$  (collective magnon mode) are:

$$\frac{d\hat{a}}{dt} = -i\omega_p \hat{a} - G_{\text{eff}} \hat{M} - \kappa_p \hat{a}, \quad (19)$$

$$\frac{d\hat{M}}{dt} = -i\omega_m \hat{M} - G_{\text{eff}} \hat{a} - \kappa_m \hat{M}. \quad (20)$$

Assuming harmonic solutions  $\hat{a}(t) = a_0 e^{-i\omega t}$ ,  $\hat{M}(t) = m_0 e^{-i\omega t}$ , we derive the matrix equation:

$$\begin{pmatrix} i(\omega_p - \omega) + \kappa_p & G_{\text{eff}} \\ G_{\text{eff}} & i(\omega_m - \omega) + \kappa_m \end{pmatrix} \begin{pmatrix} a_0 \\ b_0 \end{pmatrix} = \mathbf{0}. \quad (21)$$

Solving for eigenfrequencies gives:

$$\tilde{\omega}_{\pm} = \frac{\omega_m + \omega_p - i(\kappa_p + \kappa_m)}{2} \pm \frac{1}{2} \sqrt{[\omega_p - \omega_m - i(\kappa_m - \kappa_p)]^2 + 4G_{\text{eff}}^2}. \quad (22)$$

The real parts of  $\tilde{\omega}_{\pm}$  represent resonance frequencies, while the imaginary parts correspond to relaxation rates of the magnon-photon polaritons.

In the limit  $f_i \gg \kappa_i$  for uncoupled magnon and photon modes, the resonance frequencies  $\omega_{\pm}$  and the relaxation rates  $\kappa_{\pm}$  reduce to:

$$\omega_{\pm} = \frac{\omega_m + \omega_p}{2} \pm \frac{1}{2} \sqrt{[\omega_p - \omega_m]^2 + 4G_{\text{eff}}^2}, \quad (23)$$

$$\kappa_{\pm} = \frac{\kappa_m + \kappa_p}{2} \pm \frac{\kappa_p - \kappa_m}{2} \frac{\omega_p - \omega_m}{\sqrt{[\omega_p - \omega_m]^2 + 4G_{\text{eff}}^2}}. \quad (24)$$

Fitting experimental data for resonance frequencies and half-width at half-maximum (HWHM) enables the extraction of key parameters  $G_{\text{eff}}$ ,  $\kappa_p$ , and  $\kappa_m$ , thus identifying the coupling regime such as weak coupling, strong coupling or Purcell regime<sup>32</sup>. Extended figure 2 presents fitting results for a resonator coupled to a single permalloy stripe in YBCO#2, yielding  $G_{\text{eff}}/2\pi \approx 129 \pm 1.4$  MHz,  $\kappa_p/2\pi \approx 0.53 \pm 0.03$  MHz, and  $\kappa_m/2\pi \approx 461 \pm 11$  MHz, placing these magnon polaritons in the Purcell regime ( $\kappa_p < G < \kappa_m$ )<sup>32</sup>. Notably, the broader linewidth observed for the magnon-like branch compared with the expectation from Eq. (24) indicates a Purcell-enhanced relaxation of the photons driven by the large magnon relaxation rate in this system. Assuming  $\kappa_m$  and  $\kappa_p$  remain unchanged when multiple magnon modes couple to a single photon mode, the cooperativity  $C = G_{\text{eff}}^2/\kappa_m \kappa_p$  increases from 67.4 for one permalloy stripe to 1860 for 26 permalloy stripes. The highest cooperativity in our system surpasses previously reported values for magnon polaritons in thin ferromagnetic films coupled to superconducting resonator<sup>27,52</sup>.



## **Data availability**

The data that support the findings of this work are available from the corresponding authors upon reasonable request.

## **Acknowledgment**

This work was supported in part by the Japan Society for the Promotion of Science (JSPS) Research Fellow Program (grant no. 22KJ1956), JSPS Overseas Challenge Program for Young Researchers (grant no. 202280145), Grant-in-Aid for Scientific Research (B) (grant no. 21H01798), and the Spintronics Research Network of Japan (Spin-RNJ). SY thanks T. Hioki and J. C. Gartside for the fruitful discussions and comments on the manuscript. MM, MA, and HH acknowledge financial support by the Deutsche Forschungsgemeinschaft (DFG, German Research Foundation) via Germany's Excellence Strategy EXC-2111- 390814868 and the Transregio "Constrained Quantum Matter" (TRR 360, Project-ID 492547816). This research is part of the Munich Quantum Valley, which is supported by the Bavarian State Government with funds from the Hightech Agenda Bayern Plus.

## **Supplemental Information**

- No. 1 Evaluation of bare YBCO superconducting resonators
- No. 2 Magnetic field and temperature dependence of YBCO resonator with lumped-element structure
- No. 3 Surface image of YBCO resonators by AFM
- No. 4 Derivation of eigenfrequencies with the different type of Hamiltonians for magnon polaritons
- No. 5 Cavity-mediated coupling between permalloy elements
- No. 6 Origin of  $A^2$  term in electron-photon interactions

## Reference

1. DiCarlo, L. *et al.* Preparation and measurement of three-qubit entanglement in a superconducting circuit. *Nature* **467**, 574–578 (2010).
2. Barends, R. *et al.* Superconducting quantum circuits at the surface code threshold for fault tolerance. *Nature* **508**, 500–503 (2014).
3. Kurpiers, P. *et al.* Deterministic quantum state transfer and remote entanglement using microwave photons. *Nature* **558**, 264–267 (2018).
4. Forn-Díaz, P., Lamata, L., Rico, E., Kono, J. & Solano, E. Ultrastrong coupling regimes of light-matter interaction. *Rev. Mod. Phys.* **91**, 25005 (2019).
5. Ciuti, C., Bastard, G. & Carusotto, I. Quantum vacuum properties of the intersubband cavity polariton field. *Phys. Rev. B* **72**, 115303 (2005).
6. Emary, C. & Brandes, T. Chaos and the quantum phase transition in the Dicke model. *Phys. Rev. E* **67**, 066203 (2003).
7. Ashhab, S. & Nori, F. Qubit-oscillator systems in the ultrastrong-coupling regime and their potential for preparing nonclassical states. *Phys. Rev. A* **81**, 042311 (2010).
8. Stassi, R., Ridolfo, A., Di Stefano, O., Hartmann, M. J. & Savasta, S. Spontaneous Conversion from Virtual to Real Photons in the Ultrastrong-Coupling Regime. *Phys. Rev. Lett.* **110**, 243601 (2013).

9. De Liberato, S. Virtual photons in the ground state of a dissipative system. *Nat. Commun.* **8**, 1465 (2017).
10. Wang, Y. K. & Hioe, F. T. Phase Transition in the Dicke Model of Superradiance. *Phys. Rev. A* **7**, 831–836 (1973).
11. Hepp, K. & Lieb, E. H. On the superradiant phase transition for molecules in a quantized radiation field: the dicke maser model. *Annals of Physics* **76**, 360–404 (1973).
12. Frisk Kockum, A., Miranowicz, A., De Liberato, S., Savasta, S. & Nori, F. Ultrastrong coupling between light and matter. *Nat. Rev. Phys.* **1**, 19–40 (2019).
13. Niemczyk, T. *et al.* Circuit quantum electrodynamics in the ultrastrong-coupling regime. *Nat. Phys.* **6**, 772–776 (2010).
14. Forn-Díaz, P. *et al.* Observation of the Bloch-Siegert Shift in a Qubit-Oscillator System in the Ultrastrong Coupling Regime. *Phys. Rev. Lett.* **105**, 237001 (2010).
15. Yoshihara, F. *et al.* Superconducting qubit-oscillator circuit beyond the ultrastrong-coupling regime. *Nat. Phys.* **13**, 44–47 (2017).
16. Anappara, A. A. *et al.* Signatures of the ultrastrong light-matter coupling regime. *Phys. Rev. B* **79**, 201303 (2009).
17. Geiser, M. *et al.* Ultrastrong Coupling Regime and Plasmon Polaritons in Parabolic Semiconductor Quantum Wells. *Phys. Rev. Lett.* **108**, 106402 (2012).

18. Askenazi, B. *et al.* Midinfrared Ultrastrong Light–Matter Coupling for THz Thermal Emission. *ACS Photonics* **4**, 2550–2555 (2017).
19. Bialynicki-Birula, I. & Rzążewski, K. No-go theorem concerning the superradiant phase transition in atomic systems. *Phys. Rev. A* **19**, 301–303 (1979).
20. Nataf, P. & Ciuti, C. No-go theorem for superradiant quantum phase transitions in cavity QED and counter-example in circuit QED. *Nat. Commun.* **1**, 72 (2010).
21. Li, X. *et al.* Observation of Dicke cooperativity in magnetic interactions. *Science* **361**, 794–797 (2018).
22. Bamba, M., Li, X., Marquez Peraca, N. & Kono, J. Magnonic superradiant phase transition. *Commun. Phys.* **5**, 3 (2022).
23. Kritzell, T. E. *et al.* Zeeman polaritons as a platform for probing Dicke physics in condensed matter. Preprint at <https://doi.org/10.48550/arXiv.2409.17339> (2024).
24. Kim, D. *et al.* Observation of the Magnonic Dicke Superradiant Phase Transition. *Sci. Adv.* **11**, 1691 (2024).
25. Kubo, Y. *et al.* Strong Coupling of a Spin Ensemble to a Superconducting Resonator. *Phys. Rev. Lett.* **105**, 140502 (2010).
26. Huebl, H. *et al.* High Cooperativity in Coupled Microwave Resonator Ferrimagnetic Insulator Hybrids. *Phys. Rev. Lett.* **111**, 127003 (2013).

27. Li, Y. *et al.* Strong Coupling between Magnons and Microwave Photons in On-Chip Ferromagnet-Superconductor Thin-Film Devices. *Phys. Rev. Lett.* **123**, 107701 (2019).
28. Hou, J. T. & Liu, L. Strong Coupling between Microwave Photons and Nanomagnet Magnons. *Phys. Rev. Lett.* **123**, 107702 (2019).
29. Bloch, F. & Siegert, A. Magnetic Resonance for Nonrotating Fields. *Phys. Rev.* **57**, 522–527 (1940).
30. Goryachev, M. *et al.* High-cooperativity cavity QED with magnons at microwave frequencies. *Physical Review Applied* **2**, 1–11 (2014).
31. Ghirri, A. *et al.* Ultrastrong Magnon-Photon Coupling Achieved by Magnetic Films in Contact with Superconducting Resonators. *Phys. Rev. Appl.* **20**, 024039 (2023).
32. Zhang, X., Zou, C.-L. L., Jiang, L. & Tang, H. X. Strongly Coupled Magnons and Cavity Microwave Photons. *Phys. Rev. Lett.* **113**, 156401 (2014).
33. Li, X. *et al.* Vacuum Bloch–Siegert shift in Landau polaritons with ultra-high cooperativity. *Nature Photon* **12**, 324–329 (2018).
34. Mueller, N. S. *et al.* Deep strong light–matter coupling in plasmonic nanoparticle crystals. *Nature* **583**, 780–784 (2020).
35. Dicke, R. H. Coherence in Spontaneous Radiation Processes. *Phys. Rev.* **93**, 99–110 (1954).
36. Cohen-Tannoudji, C., Dupont-Roc, J. & Fabre, C. A quantum calculation of the higher order terms in the Bloch-Siegert shift. *J. Phys. B: At. Mol. Phys.* **6**, L214–L217 (1973).

37. Hotter, C., Miranowicz, A. & Gietka, K. Quantum Metrology in the Ultrastrong Coupling Regime of Light-Matter Interactions: Leveraging Virtual Excitations without Extracting Them. Preprint at <https://doi.org/10.48550/arXiv.2501.16304> (2025).
38. Hou, J. T., Chou, C. T., Han, J., Fan, Y. & Liu, L. Electrical manipulation of dissipation in microwave photon-magnon hybrid system through the spin Hall effect. *Appl. Phys. Lett.* **124**, (2024).
39. Lee, O. *et al.* Nonlinear Magnon Polaritons. *Phys. Rev. Lett.* **130**, 046703 (2023).
40. Zakeri, K. & von Faber, A. Giant Spin-Orbit Induced Magnon Nonreciprocity in Ultrathin Ferromagnets. *Phys. Rev. Lett.* **132**, 126702 (2024).
41. Zhang, D., Luo, X. Q., Wang, Y. P., Li, T. F. & You, J. Q. Observation of the exceptional point in cavity magnon-polaritons. *Nat. Commun.* **8**, 1–6 (2017).
42. Bai, L. *et al.* Spin Pumping in Electrodynamically Coupled Magnon-Photon Systems. *Phys. Rev. Lett.* **114**, 227201 (2015).
43. Maier-Flaig, H., Harder, M., Gross, R., Huebl, H. & Goennenwein, S. T. B. Spin pumping in strongly coupled magnon-photon systems. *Phys. Rev. B* **94**, 054433 (2016).
44. Li, Y. *et al.* Coherent Spin Pumping in a Strongly Coupled Magnon-Magnon Hybrid System. *Phys. Rev. Lett.* **124**, 117202 (2020).
45. Hioki, T., Shimizu, H., Makiuchi, T. & Saitoh, E. State tomography for magnetization dynamics. *Phys. Rev. B* **104**, L100419 (2021).

46. Haygood, I. W., Pufall, M. R., Edwards, E. R. J., Shaw, J. M. & Rippard, W. H. Strong Coupling of an Fe-Co Alloy with Ultralow Damping to Superconducting Co-Planar Waveguide Resonators. *Phys. Rev. Appl.* **15**, 054021 (2021).
47. Müller, M. *et al.* Magnetic field robust high quality factor NbTiN superconducting microwave resonators. *Materials for Quantum Technology* **2**, 015002 (2022).
48. Probst, S., Song, F. B., Bushev, P. A., Ustinov, A. V. & Weides, M. Efficient and robust analysis of complex scattering data under noise in microwave resonators. *Review of Scientific Instruments* **86**, 024706 (2015).
49. Weichselbaumer, S. *et al.* Quantitative modeling of superconducting planar resonators for electron spin resonance. *Phys. Rev. Appl.* **12**, 024021 (2019).
50. Hopfield, J. J. Theory of the Contribution of Excitons to the Complex Dielectric Constant of Crystals. *Phys. Rev.* **112**, 1555–1567 (1958).
51. Zhang, X. *et al.* Magnon dark modes and gradient memory. *Nat. Commun.* **6**, 8914 (2015).
52. Guo, S. *et al.* Strong on-Chip Microwave Photon-Magnon Coupling Using Ultralow-Damping Epitaxial Y<sub>3</sub>Fe<sub>5</sub>O<sub>12</sub> Films at 2 K. *Nano Lett.* **23**, 5055–5060 (2023).

## Figure captions

### Figure 1 | Comparison of electric dipole and magnetic dipole coupling with photons.

(a, b) Schematics of the cavity QED system composing of (a) electric dipole coupling system such as plasmon and (b) magnetic dipole coupling system such as magnon and ensemble spins coupling with photons.

### Figure 2 | On-chip magnon polaritons in the ultrastrong coupling regime and direct observation of the Bloch-Siegert shift.

(a) Schematic illustration of the lumped-element superconducting resonator with 30-nm-thick permalloy (Py) stripes, with the inset depicting the layer structure of the ferromagnetic elements.

(b) The magnitude of the transmission spectrum  $|S_{21}|$  of the bare resonator measured at 10 K and zero magnetic field. The red dashed curve is a fit via Eq. (5), see Methods.

(c) Photon absorption of the superconducting resonator incorporating multiple permalloy elements as a function of the applied magnetic field. Peaks shift clearly with varying magnetic field. The red dotted curves trace the peak positions extracted from the transmission spectra.

(d-f) Enlarged transmission spectra at low magnetic fields: (d) 0 mT, (e) 7 mT and (f) 14 mT, fitted by Eq. (5). These spectra demonstrate the subtle peak shifts attributed to magnon-photon coupling.

(g) Normalized transmission spectra  $|\Delta S_{21}|$  as a function of applied magnetic field for the resonator with multiple permalloy stripes in YBCO#1 chip. Red dashed curves represent fits based on the polariton frequencies of Eq. (2). Blue and black dashed lines indicate the uncoupled photon and magnon modes, respectively. Inset shows extracted effective coupling strength  $G_{\text{eff}}$  and the normalized coupling ratio  $\eta$ , confirming the ultrastrong coupling regime ( $\eta > 0.1$ ).

(h, i) Experimental spectra compared with simulations obtained by excluding the counter-rotating terms (CRTs) (purple dashed lines) and the diamagnetic term (orange dashed lines), for the upper (d) and lower polariton branches. Deviations induced by neglecting counter-rotating terms directly manifest as the Bloch-Siegert shift ( $\Delta f_{\text{BS}}$ ).

### Figure 3 | Dicke cooperativity of collective magnon modes

(a) Schematic illustration of the coupling between the uniform photon mode and multiple magnon modes, collectively forming the magnon bright mode. The effective coupling strength is given by  $G_{\text{eff}} = g_0\sqrt{n}$ , where  $n$  is the number of magnon modes coupled to the uniform photon mode.

(b-e) Transmission spectra of resonators (b) 1, (c) 8, (d) 16 and (e) 26 permalloy stripes in YBCO#2 as a function of the applied magnetic field.

(f) Normalized coupling strength  $\varepsilon$  as a function of  $\sqrt{n}$ , where  $n$  is the number of permalloy stripes, for both YBCO#1 and YBCO#2.

### Figure 4 | Control of Bloch-Siegert shift via the effective coupling strength of magnon polaritons.

(a) Bloch-Siegert shift  $\Delta f_{\text{BS}}$  as a function of the applied magnetic field for resonators with different numbers of permalloy stripes. The inset identifies the YBCO chip index and the corresponding stripe count.

(b) Bloch-Siegert shift as a function of the square of the normalized coupling strength  $\varepsilon$  for thin permalloy stripes, measured at applied magnetic fields of 65, 100, and 140 mT.

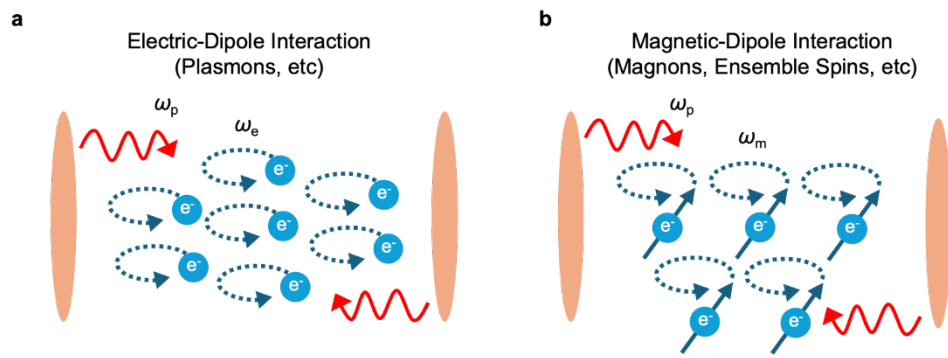


Fig. 1 Yoshii *et al.*

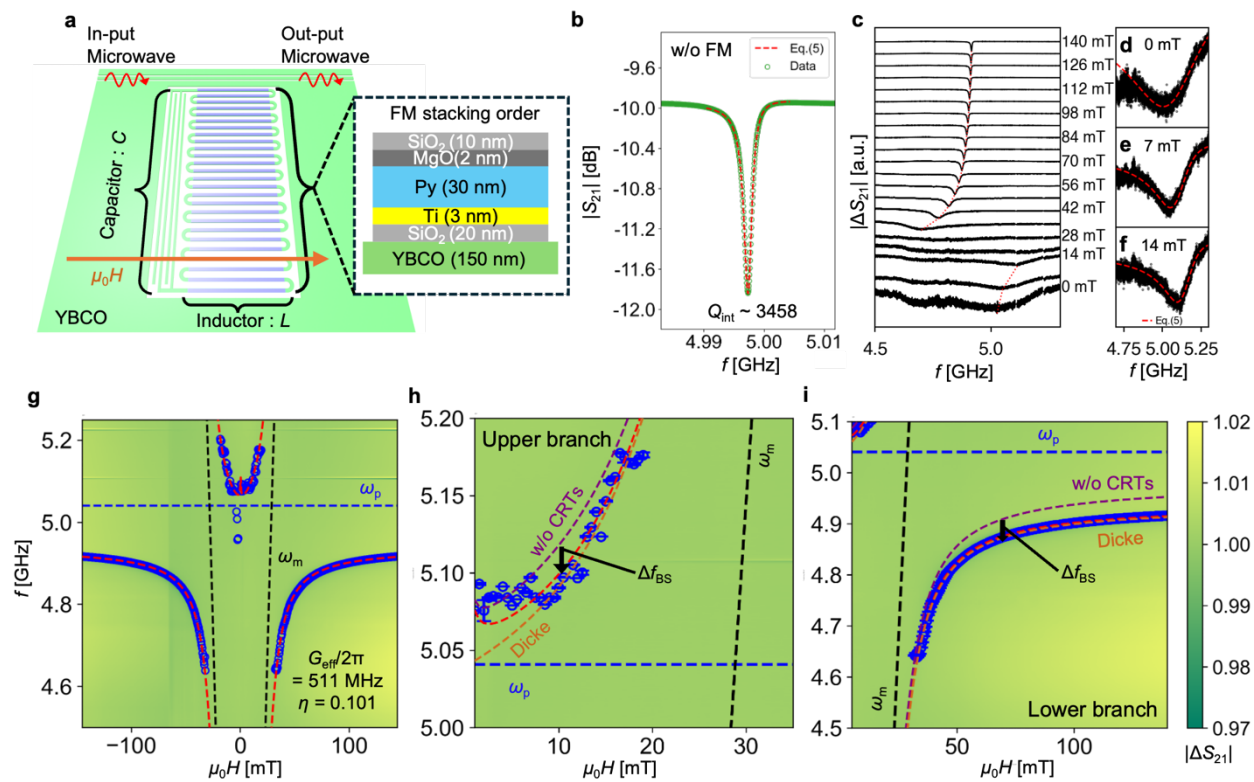


Fig. 2 Yoshii *et al.*

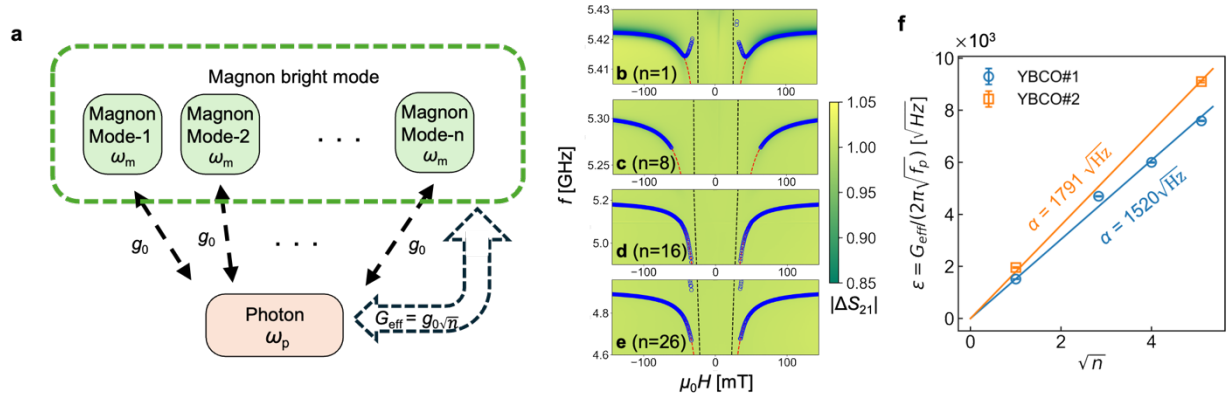


Fig. 3 Yoshii *et al.*

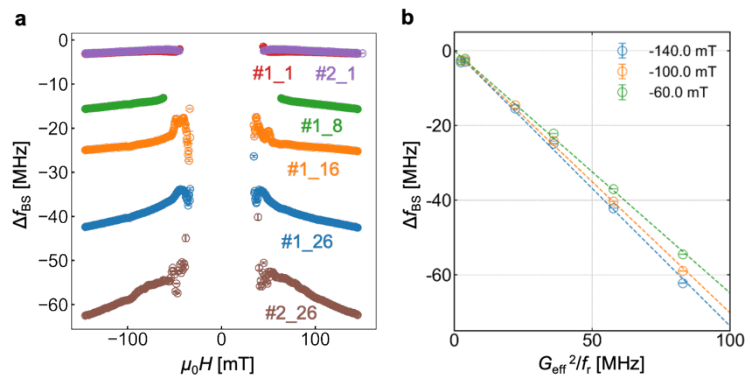
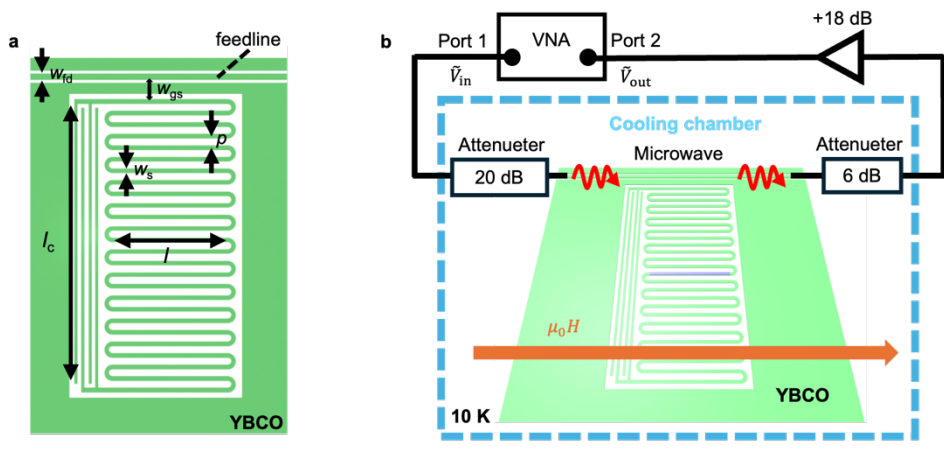


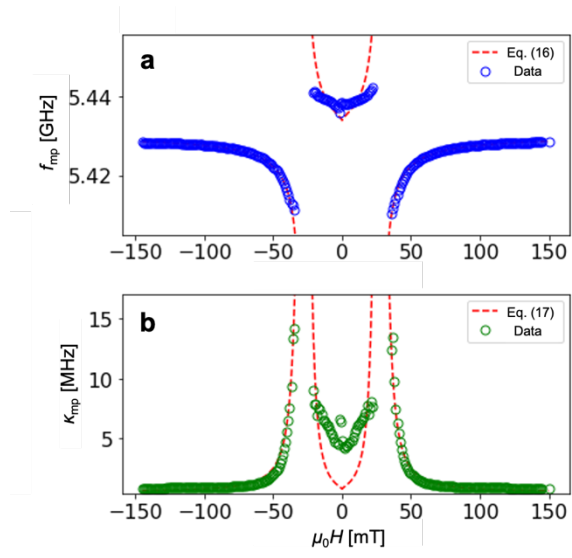
Fig. 4 Yoshii *et al.*



Extended Data Fig. 1

Resonator parameter	
$w_{fd}$	20 $\mu\text{m}$
$w_s$	15 $\mu\text{m}$
$w_{gs}$	42 $\mu\text{m}$ (YBCO#1) 72 $\mu\text{m}$ (YBCO#2)
$p$	25 $\mu\text{m}$
$l$	400 $\mu\text{m}$

Extended Table. 1



Extended Data Fig. 2